Results in Physics 8 (2018) 341–351

Contents lists available at ScienceDirect

Results in Physics

journal homepage: www.journals.elsevier.com/results-in-physics

Effect of Cattaneo-Christov heat flux on Jeffrey fluid flow with variable thermal conductivity

Tasawar Hayat [a,b], Mehwish Javed [a], Maria Imtiaz [c,*], Ahmed Alsaedi [b]

[a] Department of Mathematics, Quaid-I-Azam University, 45320 Islamabad 44000, Pakistan
[b] Nonlinear Analysis and Applied Mathematics (NAAM) Research Group, Department of Mathematics, Faculty of Science, King Abdulaziz University, Jeddah 21589, Saudi Arabia
[c] Department of Mathematics, University of Wah, Wah Cantt 47040, Pakistan

ARTICLE INFO

Article history:
Received 3 August 2017
Received in revised form 21 October 2017
Accepted 3 December 2017
Available online 15 December 2017

Keywords:
Cattaneo-Christov heat flux model
Jeffrey fluid
Variable thickness
Variable thermal conductivity

ABSTRACT

This paper presents the study of Jeffrey fluid flow by a rotating disk with variable thickness. Energy equation is constructed by using Cattaneo-Christov heat flux model with variable thermal conductivity. A system of equations governing the model is obtained by applying boundary layer approximation. Resulting nonlinear partial differential system is transformed to ordinary differential system. Homotopy concept leads to the convergent solutions development. Graphical analysis for velocities and temperature is made to examine the influence of different involved parameters. Thermal relaxation time parameter signifies that temperature for Fourier's heat law is more than Cattaneo-Christov heat flux. A constitutional analysis is made for skin friction coefficient and heat transfer rate. Effects of Prandtl number on temperature distribution and heat transfer rate are scrutinized. It is observed that larger Reynolds number gives illustrious temperature distribution.

Introduction

Non-Newtonian fluids have emerging applications in numerous fields. There is no linear relation between deformation and stress tensor in such materials. Examples of such fluids are custard, toothpaste, blood, petroleum and slurry etc. The flow of non-Newtonian fluids cannot be simulated by the Navier Stokes equations. Plastic extrusion is a one example of such embarrassing deficiency. The constitutive equations of non-Newtonian fluids are usually too complex to solve because of high nonlinearity than Navier-Stokes equations. Non-Newtonian fluids have three classes namely rate, integral and differential. Considered model of Jeffrey fluid is a sub-class of rate type fluids which deal with retardation time and ratio of relaxation to retardation times. Several scientists have worked with different flow models of non-Newtonian fluids [1–12].

Flow by rotating disk is quite popular in present. It is due to its demand in various scientific application related to engineering such as turbines and motor rotor system etc. Different fields like fluid dynamics of cosmology, geophysics and astrophysics are employing the auspicious applications of rotating flows. Full governing equations of such kind of flows were initially transformed to accessible form by Von Karman [13]. Cochran [14] worked numerically for these equations. Solution of energy equation for rotating flow problem was found by Pohlhausen and Millsaps [15]. Turkyilmazoglu [16] analyzed heat transfer in flow by two stretchable rotating disks. Axisymmetric MHD flow of Jeffrey fluid by a rotating disk is explored by Hayat et al. [17]. Ming et al. [18] discussed heat transfer with double diffusion in rotating flow of power law fluid. Guha and Sengupta [19] investigated nonlinear interaction of mixed convection with Von Karman swirling flow of a heated rotating disk. Srinivas [20] explored MHD viscous fluid flow induced by contracting and expanding rotating disk with viscous dissipation. Radiative flow of carbon nanotubes generated by two stretchable rotating disks with convective boundary condition is studied by Imtiaz et al. [21].

It is known that heat transfer process occurs when temperature of body or different parts of body is not same. This process has vast applications in nuclear fusion, power generation and various engineering fields. Fourier [22] proposed the conduction law of heat which is mostly used in the past. However this law corresponds to instantaneous change of heat. It yields parabolic heat equation. This law is modified by Cattaneo [23] by adding the thermal relaxation time factor. Paradox of heat conduction is overcome by this term. This theory is further modified by Christov [24] by replacing

* Corresponding author.
E-mail address: maria.imtiaz@uow.edu.pk (M. Imtiaz).

https://doi.org/10.1016/j.rinp.2017.12.007
2211-3797/

time derivative with Oldroyd upper convected derivative. Hayat et al. [25] made a comparative study for flow of viscoelastic nanofluids using Cattaneo-Christov double diffusion model. Liu et al. [26] derived an improved heat conduction model with Riesz fractional Cattaneo–Christov flux. Meraj et al. [27] reported how Darcy-Forchheimer flow of variable conductivity influence the Jeffrey fluid through Cattaneo-Christov heat flux model. Reddy et al. [28] investigated the cross diffusion effects by considering the energy equation using Cattaneo-Christov heat flux. Ramesh et al. [29] gave an analysis of heat transfer in Magnetohydrodynamic Casson fluid flow using Cattaneo-Christov heat diffusion theory. Hadad [30] employed heat flux model to analyze thermal instability in porous medium. Hayat et al. [31] studied flow bounded by a surface of variable thickness using Cattaneo-Christov expression. Abbasi and Shehzad [32] showed how heat transfer for three dimensional Maxwell fluid with variable thermal conductivity by employing Cattaneo-Christov heat flux model. Abbasi et al. [33] made analytical study of Cattaneo-Christov heat flux model of a non-Newtonian fluid for a boundary layer flow. Cattaneo-Christov heat flux model for Darcy-Forchheimer flow with variable conductivity of an Oldroyd-B fluid was considered by Shehzad et al. [34].

No doubt variable thickness of different surfaces has incredible role for the analysis of various attributes in engineering particularly mechanical, architectural and aeronautical processes. This concept yields reduction in structural weight of elements. Eftekhari and Jafari [35] adopted accurate variational approach for free vibration of variable thickness thin and thick plates with edges elastically restrained against translation and rotation. Fang et al. [36] inspected the boundary layer flow bounded by a variable thicked stretching sheet.

This article presents the flow of Jeffrey fluid by a rotating disk with variable thickness. Heat transfer analysis is made by constructing the energy equation with Cattaneo-Christov heat flux model. This discussion is useful in different engineering fields, chemistry, polymer industry and astrophysics because variable thermal conductivity is adopted to analyze the flow. This property makes the model quite flexible as this is significant to control the temperature of the system. Convergent solutions of interest are developed. Such solutions are derived using homotopy analysis method (HAM) [37–40]. Physical quantities describing the worth of present attempt are displayed and analyzed.

Formulation

Let us consider steady laminar flow of Jeffrey fluid with variable thermal conductivity. The flow is generated by a rotating disk of variable thickness at $z = a\left(\frac{r}{R_0}+1\right)^{-m}$. Disk rotates along z-axis with prescribed angular velocity Ω. The disk is maintained at constant temperature T_w whereas T_∞ is the ambient fluid temperature. The velocity field $\mathbf{V} = [u(r,\theta,z), v(r,\theta,z), w(r,\theta,z)]$ and temperature field $T = T(r,\theta,z)$ with assumptions $\frac{\partial p}{\partial r} = \frac{\partial p}{\partial z} = 0$ are taken into consideration. Equations governing present consideration are

$$\frac{\partial u}{\partial r} + \frac{u}{r} + \frac{\partial w}{\partial z} = 0, \tag{1}$$

$$u\frac{\partial u}{\partial r} - \frac{v^2}{r} + w\frac{\partial u}{\partial z} = \frac{\nu}{1+\lambda_1}\frac{\partial^2 u}{\partial z^2} + \frac{\lambda_2 \nu}{1+\lambda_1}\left[2u\frac{\partial^3 u}{\partial r\partial z^2} + 2w\frac{\partial^3 u}{\partial z^3} + \frac{\partial u}{\partial z}\frac{\partial^2 u}{\partial r\partial z} + \frac{\partial w}{\partial z}\frac{\partial^2 u}{\partial z^2}\right], \tag{2}$$

$$u\frac{\partial v}{\partial r} + \frac{uv}{r} + w\frac{\partial v}{\partial z} = \frac{\nu}{1+\lambda_1}\frac{\partial^2 v}{\partial z^2} + \frac{\lambda_2 \nu}{1+\lambda_1}\left[2u\frac{\partial^3 v}{\partial r\partial z^2} + \frac{\partial u}{\partial z}\frac{\partial^2 v}{\partial r\partial z} + 2w\frac{\partial^3 v}{\partial z^3} + \frac{\partial w}{\partial z}\frac{\partial^2 v}{\partial z^2}\right], \tag{3}$$

$$\rho C_p\left(\frac{\partial T}{\partial t} + (\mathbf{V}\cdot\nabla)T\right) = -\nabla\cdot\mathbf{q}, \tag{4}$$

where u, v and w are the velocity components along r, θ and z directions respectively, ν is the kinematic viscosity, ρ is the density of fluid, σ is electrical conductivity, λ_1 is the ratio of relaxation to retardation time, λ_2 is retardation time, T is temperature of fluid, C_p is specific heat and $\mathbf{q}$ is the heat flux satisfying

$$\mathbf{q} + \lambda\left[\frac{\partial \mathbf{q}}{\partial t} + \mathbf{v}\cdot\nabla\mathbf{q} - \mathbf{q}\cdot\nabla\mathbf{v} + (\nabla\cdot\mathbf{v})\mathbf{q}\right] = -K(T)\nabla T, \tag{5}$$

where λ is the thermal relaxation time and $K(T)$ is the variable thermal conductivity. For incompressible fluid case one has

$$\mathbf{q} + \lambda\left[\frac{\partial \mathbf{q}}{\partial t} + \mathbf{v}\cdot\nabla\mathbf{q} - \mathbf{q}\cdot\nabla\mathbf{v}\right] = -K(T)\nabla T. \tag{6}$$

Elimination of $\mathbf{q}$ yields

$$u\frac{\partial T}{\partial r} + w\frac{\partial T}{\partial z} = \frac{K}{\rho C_p}\frac{\partial^2 T}{\partial z^2} + \frac{1}{\rho C_p}\frac{\partial K}{\partial z}\frac{\partial T}{\partial z} - \lambda\left[u^2\frac{\partial^2 T}{\partial r^2} + w^2\frac{\partial^2 T}{\partial z^2} + 2uw\frac{\partial^2 T}{\partial r\partial z} + \left(u\frac{\partial u}{\partial r} + w\frac{\partial u}{\partial z}\right)\frac{\partial T}{\partial r} + \left(u\frac{\partial w}{\partial r} + w\frac{\partial w}{\partial z}\right)\frac{\partial T}{\partial z}\right]. \tag{7}$$

Boundary conditions of present problem are

$$u = 0, \quad v = r\Omega, \quad w = 0, \quad T = T_w \text{ as } z = a\left(\frac{r}{R_0}+1\right)^{-m}, \tag{8}$$

$$u \to 0, \quad v \to 0, \quad T \to T_\infty \text{ as } z \longrightarrow \infty. \tag{9}$$

Invoking the transformations

$$u = r^* R_0\Omega F(\eta), \quad v = r^* R_0\Omega G(\eta), \quad w = R_0\Omega(1+r^*)^{-m}\left(\frac{\Omega R_0^2\rho}{\mu}\right)^{\frac{-1}{n+1}} J(\eta),$$
$$\Theta(\eta) = \frac{T - T_\infty}{T_w - T_\infty}, \quad K = k_\infty(1+\epsilon\Theta), \quad \eta = \frac{z}{R_0}\left(\frac{\Omega R_0^2\rho}{\mu}\right)^{\frac{1}{n+1}}(1+r^*)^m. \tag{10}$$

Eqs. (1)–(3) and (7)–(9) become

$$2F + m\epsilon\eta F' + J' = 0, \tag{11}$$

$$(\mathrm{Re})^{\frac{1-n}{1+n}}(1+r^*)^{2m}F'' + \beta(\mathrm{Re})^{\frac{1-n}{1+n}}(1+r^*)^{2m}\left[2FF'' + 4m\psi FF'' + 2m\psi\eta FF''' + 2F'''J + F'^2 + m\psi F'^2 + m\psi\eta F'F'' + J'F''\right] - (1+\lambda_1)\left[F^2 + m\psi\eta FF' - G^2 + JF'\right] = 0, \tag{12}$$

$$(\mathrm{Re})^{\frac{1-n}{1+n}}(1+r^*)^{2m}G'' + \beta(\mathrm{Re})^{\frac{1-n}{1+n}}(1+r^*)^{2m}\left[2FG'' + 4m\psi FG'' + 2m\psi\eta FG''' + F'G' + m\psi F'G' + m\psi\eta F'G'' + 2G'''H + J'G''\right] - (1+\lambda_1)\left[2FG + m\psi\eta FG' + JG'\right] = 0, \tag{13}$$

$$\frac{1}{\Pr}(\mathrm{Re})^{\frac{1-n}{1+n}}(1+r^*)^{2m}(1+\epsilon\Theta)\Theta''+\frac{1}{\Pr}(\mathrm{Re})^{\frac{1-n}{1+n}}(1+r^*)^{2m}\epsilon\Theta'^2 - m\psi\eta F\Theta' - J\Theta' - \gamma\Big[m(m-1)\psi^2\eta F^2\Theta' + m^2\eta^2\psi^2F^2\Theta'' + J^2\Theta'' + m\psi\eta F^2\Theta' + m^2\eta^2\psi^2FF'\Theta' + m\psi\eta F'J\Theta' + m\psi\eta F\Theta'J' + JJ'\Theta'\Big] = 0, \tag{14}$$

with boundary conditions

$$F(\alpha)=0,\quad G(\alpha)=1,\quad J(\alpha)=0,\quad \Theta(\alpha)=1, \tag{15}$$

$$F(\infty)=0,\quad G(\infty)=0,\quad \Theta(\infty)=0. \tag{16}$$

where $r^*=\frac{r}{R_0}$ is the dimensionless radius, $\psi=\frac{r^*}{1+r^*}$ is the dimensionless constant, k_∞ is the thermal conductivity of ambient fluid, ϵ is a scaler parameter and Θ is dimensionless temperature. Employing another set of transformations

$$F=f(\eta-\alpha)=f(\xi),\quad G=g(\eta-\alpha)=g(\xi),$$
$$J=j(\eta-\alpha)=j(\xi),\quad \Theta=\theta(\eta-\alpha)=\theta(\xi), \tag{17}$$

Eqs. (11)–(16) are converted to

$$2f+m\epsilon(\xi+\alpha)f'+j'=0, \tag{18}$$

$$(\mathrm{Re})^{\frac{1-n}{1+n}}(1+r^*)^{2m}f''+\beta(\mathrm{Re})^{\frac{1-n}{1+n}}(1+r^*)^{2m}\big[2ff''+4m\psi ff'' + 2m\psi(\xi+\alpha)ff'''+2f'''j+f'^2+m\psi f'^2+m\psi(\xi+\alpha)f'f''+j'f''\big] - (1+\lambda_1)\Big[f^2+m\psi(\xi+\alpha)ff'-g^2+jf'\Big]=0, \tag{19}$$

$$(\mathrm{Re})^{\frac{1-n}{1+n}}(1+r^*)^{2m}g''+\beta(\mathrm{Re})^{\frac{1-n}{1+n}}(1+r^*)^{2m}\big[2fg''+4m\psi fg'' + 2m\psi(\xi+\alpha)fg'''+f'g'+m\psi f'g'+m\psi(\xi+\alpha)f'g''+2g'''j+j'g''\big] - (1+\lambda_1)\big[2fg+m\psi(\xi+\alpha)fg'+jg'\big]=0, \tag{20}$$

$$\frac{1}{\Pr}(\mathrm{Re})^{\frac{1-n}{1+n}}(1+r^*)^{2m}(1+\epsilon\theta)\theta''+\frac{1}{\Pr}(\mathrm{Re})^{\frac{1-n}{1+n}}(1+r^*)^{2m}\epsilon\theta'^2 - m\psi(\xi+\alpha)f\theta'-j\theta'-\gamma\Big[m(m-1)\psi^2(\xi+\alpha)f^2\theta' + m^2(\xi+\alpha)^2\psi^2f^2\theta''+j^2\theta''+m\psi(\xi+\alpha)f^2\theta'+m^2(\xi+\alpha)^2\psi^2ff'\theta' + m\psi(\xi+\alpha)f'j\theta'+m\psi(\xi+\alpha)f\theta'j'+jj'\theta'\Big]=0, \tag{21}$$

$$f(0)=0,\quad g(0)=1,\quad j(0)=0,\quad \theta(0)=1, \tag{22}$$

$$f(\infty)=0,\quad g(\infty)=0,\quad \theta(\infty)=0, \tag{23}$$

where m is the thickness index of disk, n is power law exponent of fluid, α is dimensionless coefficient of thickness index, Pr is Prandtl number, γ is thermal relaxation time, Re is Reynolds number and β is Deborah number. These parameters are interpreted as

$$\Pr=\frac{\rho c_p v}{k_\infty},\quad \mathrm{Re}=\frac{\Omega R_0^2\rho}{\mu},\quad \gamma=\lambda\Omega,\quad \beta=\lambda_2\Omega,$$
$$\alpha=\frac{a}{R_0}\left(\frac{\Omega R_0^2\rho}{\mu}\right)^{\frac{1}{n+1}}. \tag{24}$$

Skin friction coefficients in radial and azimuthal directions C_f and C_g are

$$C_f=\frac{\tau_{rz}\big|_{z=a\left(1+\frac{r}{R_0}\right)^m}}{\rho(\Omega R_0)^2}, \tag{25}$$

$$C_g=\frac{\tau_{\theta z}\big|_{z=a\left(1+\frac{r}{R_0}\right)^m}}{\rho(\Omega R_0)^2}, \tag{26}$$

where τ_{rz} and $\tau_{\theta z}$ are shear stresses in radial and azimuthal directions given by

$$\tau_{rz}=\frac{\mu}{1+\lambda_1}\left[\frac{\partial u}{\partial z}+\lambda_2\left(u\frac{\partial}{\partial r}+w\frac{\partial}{\partial z}\right)\frac{\partial u}{\partial z}\right], \tag{27}$$

$$\tau_{\theta z}=\frac{\mu}{1+\lambda_1}\left[\frac{\partial v}{\partial z}+\lambda_2\left(u\frac{\partial}{\partial r}+w\frac{\partial}{\partial z}\right)\frac{\partial v}{\partial z}\right]. \tag{28}$$

The dimensionless forms of skin friction coefficients are

$$\mathrm{Re}^{\frac{n}{n+1}}C_f=\frac{r^*(1+r^*)^m}{(1+\lambda_1)}\big[f'(0)+\beta(f(0)f'(0)+m\psi f(0)f'(0) + m\psi(\xi+\alpha)f(0)f''(0)+j(0)f''(0))\big], \tag{29}$$

$$\mathrm{Re}^{\frac{n}{n+1}}C_g=\frac{r^*(1+r^*)^m}{(1+\lambda_1)}[g'(0)+\beta(f(0)g'(0)+m\psi f(0)g'(0) + m\psi(\xi+\alpha)f(0)g''(0)+j(0)g''(0))], \tag{30}$$

Nusselt number for the disk is

$$Nu_r=\frac{rq_w}{K(T)(T_w-T_\infty)}\bigg|_{z=a\left(\frac{r}{R_0}+1\right)^{-m}}, \tag{31}$$

where q_w is the heat flux defined as

$$q_w\big|_{z=a\left(\frac{r}{R_0}+1\right)^{-m}}=-K(T)\frac{\partial T}{\partial z} = -k_\infty(1+\epsilon\theta(0))(T_w-T_\infty)(\mathrm{Re})^{\frac{1}{n+1}}(1+r^*)^m\frac{\theta'(0)}{R_0}. \tag{32}$$

Thus dimensionless form of heat transfer is given by

$$\mathrm{Re}^{\frac{-1}{n+1}}Nu_r=-r^*(1+r^*)^m\frac{(1+\epsilon\theta(0))\theta'(0)}{1+\epsilon\theta(0)}. \tag{33}$$

Homotopic solutions

Zeroth-order deformation equations

The system of Eqs. (18)–(21) can be solved with above mentioned boundary conditions (22)–(23). The initial guesses are

$$j_0(\xi)=0,\quad f_0(\xi)=0,\quad g_0(\xi)=\exp(-\xi),\quad \theta_0(\xi)=\exp(-\xi), \tag{34}$$

and the linear operators are

$$\mathcal{L}_j=j',\quad \mathcal{L}_f=f''-f,\quad \mathcal{L}_g=g''-g,\quad \mathcal{L}_\theta=\theta''-\theta,\quad \mathcal{L}_\phi=\phi''-\phi, \tag{35}$$

with the properties

$$\mathcal{L}_j[a_0]=0,$$
$$\mathcal{L}_f\left[a_1e^{\xi}+a_2e^{-\xi}\right]=0,$$
$$\mathcal{L}_g\left[a_3e^{\xi}+a_4e^{-\xi}\right]=0,$$
$$\mathcal{L}_\theta\left[a_5e^{\xi}+a_6e^{-\xi}\right]=0 \tag{36}$$

in which a_i ($i=0$–6) are the constants.

Let $q\in[0,1]$ represents the embedding parameter then the generalized homotopic solutions with non-zero auxiliary parameters $\hbar_j$, $\hbar_f$, $\hbar_g$ and $\hbar_\theta$ are

$$(1-q)\mathcal{L}_j[J(\xi,q)-j_0(\xi)]=q\hbar_j\mathcal{N}_j[J(\xi,q),F(\xi,q)], \tag{37}$$

$$(1-q)\mathcal{L}_f[F(\xi,q)-f_0(\xi)]=q\hbar_f\mathcal{N}_f[F(\xi,q),G(\xi,q)], \tag{38}$$

$$(1-q)\mathcal{L}_g[G(\xi,q)-g_0(\xi)]=q\hbar_g\mathcal{N}_g[G(\xi,q),F(\xi,q)], \tag{39}$$

$$(1-q)\mathcal{L}_\theta[\Theta(\xi,q)-\theta_0(\xi)]=q\hbar_\theta\mathcal{N}_\theta[\Theta(\xi,q),F(\xi,q),J(\xi,q)], \tag{40}$$

with boundary conditions

$$J(0,q)=0,\quad F(0,q)=0,\quad F(\infty,q)=0, \tag{41}$$

$$G(0,q)=1,\quad G(\infty,q)=0, \tag{42}$$

$$\theta(0,q)=1,\quad \theta(\infty,q)=0, \tag{43}$$

where $\mathcal{N}_j$, $\mathcal{N}_f$, $\mathcal{N}_g$ and $\mathcal{N}_\theta$ particularize the non-linear differential operators

$$\mathcal{N}_j=\frac{\partial J(\xi,q)}{\partial\xi}+2F(\xi,q)+m\psi(\xi+\alpha)\frac{\partial F(\xi,q)}{\partial\xi}, \tag{44}$$

$$\begin{aligned}\mathcal{N}_f=&(\mathrm{Re})^{\frac{1-n}{1+n}}(1+r^*)^{2m}\frac{\partial^2F(\xi,q)}{\partial\xi^2}\\&+\beta(\mathrm{Re})^{\frac{1-n}{1+n}}(1+r^*)^{2m}\left[2F(\xi,q)\frac{\partial^2F(\xi,q)}{\partial^2\xi}+4m\psi F(\xi,q)\frac{\partial^2F(\xi,q)}{\partial^2\xi}\right.\\&+2m\psi(\xi+\alpha)F(\xi,q)\frac{\partial^3F(\xi,q)}{\partial^3\xi}+2\frac{\partial^3F(\xi,q)}{\partial^3\xi}J(\xi,q)+\left(\frac{\partial F(\xi,q)}{\partial\xi}\right)^2\\&\left.+m\psi\left(\frac{\partial F(\xi,q)}{\partial\xi}\right)^2+m\psi(\xi+\alpha)\frac{\partial F(\xi,q)}{\partial\xi}\frac{\partial^2F(\xi,q)}{\partial^2\xi}+\frac{\partial J(\xi,q)}{\partial\xi}\frac{\partial^2F(\xi,q)}{\partial^2\xi}\right]\\&-(1+\lambda_1)\left[(F(\xi,q))^2+m\psi(\xi+\alpha)F(\xi,q)\frac{\partial F(\xi,q)}{\partial\xi}\right.\\&\left.-(G(\xi,q))^2+\frac{\partial F(\xi,q)}{\partial\xi}J(\xi,q)\right],\end{aligned} \tag{45}$$

$$\begin{aligned}\mathcal{N}_g=&(\mathrm{Re})^{\frac{1-n}{1+n}}(1+r^*)^{2m}\frac{\partial^2G(\xi,q)}{\partial\xi^2}\\&+\beta(\mathrm{Re})^{\frac{1-n}{1+n}}(1+r^*)^{2m}\left[2F(\xi,q)\frac{\partial^2G(\xi,q)}{\partial^2\xi}+4m\psi F(\xi,q)\frac{\partial^2G(\xi,q)}{\partial^2\xi}\right.\\&+2m\psi(\xi+\alpha)F(\xi,q)\frac{\partial^3G(\xi,q)}{\partial^3\xi}+2\frac{\partial^3G(\xi,q)}{\partial^3\xi}J(\xi,q)\\&+\frac{\partial F(\xi,q)}{\partial\xi}\frac{\partial G(\xi,q)}{\partial\xi}+m\psi\frac{\partial F(\xi,q)}{\partial\xi}\frac{\partial G(\xi,q)}{\partial\xi}\\&\left.+m\psi(\xi+\alpha)\frac{\partial F(\xi,q)}{\partial\xi}\frac{\partial^2G(\xi,q)}{\partial^2\xi}+\frac{\partial J(\xi,q)}{\partial\xi}\frac{\partial^2G(\xi,q)}{\partial^2\xi}\right]\\&-(1+\lambda_1)\left[2F(\xi,q)G(\xi,q)+m\psi(\xi+\alpha)F(\xi,q)\frac{\partial G(\xi,q)}{\partial\xi}\right.\\&\left.+\frac{\partial G(\xi,q)}{\partial\xi}J(\xi,q)\right],\end{aligned} \tag{46}$$

$$\begin{aligned}\mathcal{N}_\theta=&\frac{1}{\mathrm{Pr}}(\mathrm{Re})^{\frac{1-n}{1+n}}(1+r^*)^{2m}(1+\epsilon\theta)\frac{\partial^2\Theta(\xi,q)}{\partial\xi^2}\\&+\frac{1}{\mathrm{Pr}}(\mathrm{Re})^{\frac{1-n}{1+n}}(1+r^*)^{2m}\epsilon\left(\frac{\partial\Theta(\xi,q)}{\partial\xi}\right)^2\\&-m\psi(\xi+\alpha)F(\xi,q)\frac{\partial\Theta(\xi,q)}{\partial\xi}-J(\xi,q)\frac{\partial\Theta(\xi,q)}{\partial\xi}\\&-\gamma\left[m(m-1)\psi^2(\xi+\alpha)(F(\xi,q))^2\frac{\partial\Theta(\xi,q)}{\partial\xi}\right.\\&+m^2(\xi+\alpha)^2\psi^2(F(\xi,q))^2\frac{\partial^2\Theta(\xi,q)}{\partial\xi^2}+(J(\xi,q))^2\frac{\partial^2\Theta(\xi,q)}{\partial\xi^2}\\&+m\psi(\xi+\alpha)(F(\xi,q))^2\frac{\partial\Theta(\xi,q)}{\partial\xi}\\&+m^2(\xi+\alpha)^2\psi^2F(\xi,q)\frac{\partial F(\xi,q)}{\partial\xi}\frac{\partial\Theta(\xi,q)}{\partial\xi}\\&+m\psi(\xi+\alpha)\frac{\partial F(\xi,q)}{\partial\xi}J(\xi,q)\frac{\partial\Theta(\xi,q)}{\partial\xi}\\&\left.+m\psi(\xi+\alpha)F(\xi,q)\frac{\partial\Theta(\xi,q)}{\partial\xi}\frac{\partial J(\xi,q)}{\partial\xi}+J(\xi,q)\frac{\partial J(\xi,q)}{\partial\xi}\frac{\partial\Theta(\xi,q)}{\partial\xi}\right].\end{aligned} \tag{47}$$

mth order deformation equations

The mth order deformation problems are

$$\mathcal{L}_j[j_m(\xi)-\chi_m j_{m-1}(\xi)]=\hbar_j\mathcal{R}_{j,m}(\xi), \tag{48}$$

$$\mathcal{L}_f[f_m(\xi)-\chi_m f_{m-1}(\xi)]=\hbar_f\mathcal{R}_{f,m}(\xi), \tag{49}$$

$$\mathcal{L}_g[g_m(\xi)-\chi_m g_{m-1}(\xi)]=\hbar_g\mathcal{R}_{g,m}(\xi), \tag{50}$$

$$\mathcal{L}_\theta[\theta_m(\xi)-\chi_m\theta_{m-1}(\xi)]=\hbar_\theta\mathcal{R}_{\theta,m}(\xi). \tag{51}$$

Here the functions $\mathcal{R}_{j,m}(\xi)$, $\mathcal{R}_{f,m}(\xi)$, $\mathcal{R}_{g,m}(\xi)$ and $\mathcal{R}_{\theta,m}(\xi)$ attain the forms:

$$\mathcal{R}_{j,m}(\xi)=j'_{m-1}+m\psi(\xi+\alpha)f'_{m-1}+2f_{m-1}, \tag{52}$$

$$\begin{aligned}\mathcal{R}_{f,m}(\xi)=&(\mathrm{Re})^{\frac{1-n}{1+n}}(1+r^*)^{2m}f''_{m-1}\\&+\beta(\mathrm{Re})^{\frac{1-n}{1+n}}(1+r^*)^{2m}\sum_{k=0}^{m-1}\left[2f''_{m-1-k}f_k+4m\psi f''_{m-1-k}f_k\right.\\&+2m\psi(\xi+\alpha)f'''_{m-1-k}f_k+2f'''_{m-1-k}j_k+f'^2_{m-1}+m\psi f'^2_{m-1}\\&\left.+m\psi(\xi+\alpha)f'''_{m-1-k}f_k+f''_{m-1-k}j'_k\right]\\&-(1+\lambda_1)\sum_{k=0}^{m-1}\left[f^2_{m-1}+m\psi(\xi+\alpha)f'_{m-1-k}f_k-g^2_{m-1}+f'_{m-1-k}j_k\right],\end{aligned} \tag{53}$$

$$\begin{aligned}\mathcal{R}_{g,m}(\xi)=&(\mathrm{Re})^{\frac{1-n}{1+n}}(1+r^*)^{2m}g''_{m-1}\\&+\beta(\mathrm{Re})^{\frac{1-n}{1+n}}(1+r^*)^{2m}\sum_{k=0}^{m-1}\left[2g''_{m-1-k}f_k+4m\psi g''_{m-1-k}f_k\right.\\&+2m\psi(\xi+\alpha)g'''_{m-1-k}f_k+2g'''_{m-1-k}j_k+f'_{m-1-k}g'_k\\&\left.+m\psi f'_{m-1-k}g'_k+m\psi(\xi+\alpha)g''_{m-1-k}f'_k+g''_{m-1-k}j'_k\right]\\&-(1+\lambda_1)\sum_{k=0}^{m-1}\left[2f_{m-1-k}g_k+m\psi(\xi+\alpha)g'_{m-1-k}f_k+g'_{m-1-k}j_k\right],\end{aligned} \tag{54}$$

$$\begin{aligned}\mathcal{R}_{\theta,m}(\xi)=&\frac{1}{\mathrm{Pr}}(\mathrm{Re})^{\frac{1-n}{1+n}}(1+r^*)^{2m}(1+\epsilon\theta)\theta''_{m-1}\\&+\frac{1}{\mathrm{Pr}}(\mathrm{Re})^{\frac{1-n}{1+n}}(1+r^*)^{2m}\epsilon\sum_{k=0}^{m-1}\theta'_{m-1-k}\theta'_k-\sum_{k=0}^{m-1}\theta'_{m-1-k}j_k\\&-m\psi(\xi+\alpha)\sum_{k=0}^{m-1}\theta'_{m-1-k}f_k\\&-\gamma\sum_{k=0}^{m-1}\left[m(m-1)\psi^2(\xi+\alpha)\theta'_{m-1-k}\sum_{h=0}^{k}f_hf_{k-h}\right.\\&+\theta''_{m-1-k}\sum_{h=0}^{k}j_hj_{k-h}+m^2(\xi+\alpha)^2\psi^2\theta''_{m-1-k}\sum_{h=0}^{k}f_hf_{k-h}\\&+m\psi(\xi+\alpha)\theta'_{m-1-k}\sum_{h=0}^{k}f_hf_{k-h}+m\psi(\xi+\alpha)\theta'_{m-1-k}\sum_{h=0}^{k}j_hf'_{k-h}\\&+\theta'_{m-1-k}\sum_{h=0}^{k}j_hj'_{k-h}+m^2(\xi+\alpha)^2\psi^2\theta'_{m-1-k}\sum_{h=0}^{k}f_hf'_{k-h}\\&\left.+m\psi(\xi+\alpha)\theta'_{m-1-k}\sum_{h=0}^{k}f_hj'_{k-h}\right],\end{aligned} \tag{55}$$

$$\chi_m=\begin{cases}0, & m\leqslant 1\\ 1, & m>1\end{cases}. \tag{56}$$

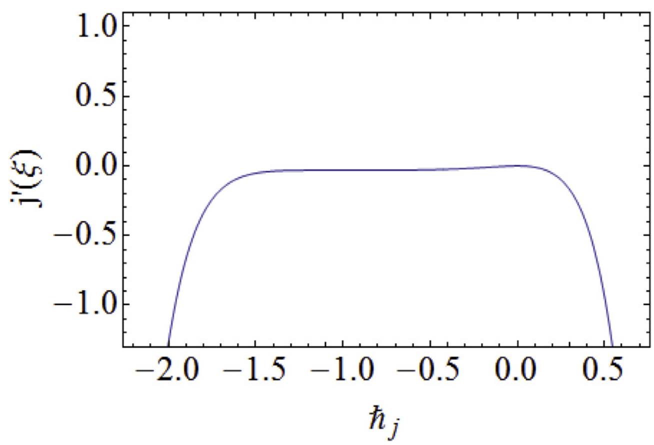

Fig. 1. $\hbar$-curve for $j'(\xi)$ when $n = \mathrm{Re} = m = 1$, $\psi = \epsilon = \gamma = 0.40$, $\alpha = 0.15$, $r^* = 0.2$, $\mathrm{Pr} = 1.5$, $\lambda_1 = 0.5$ and $\beta = 0.25$.

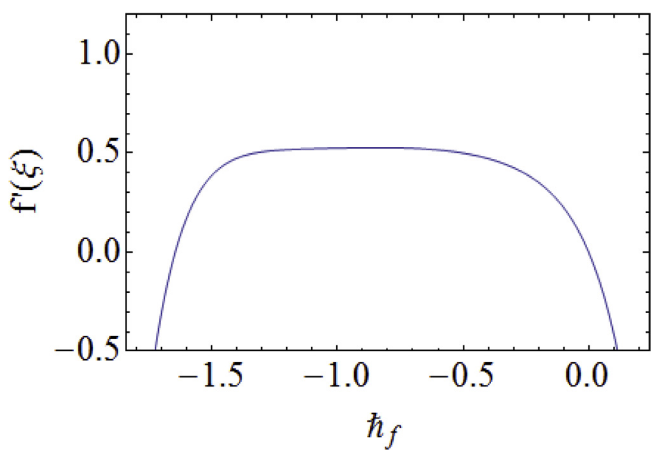

Fig. 2. $\hbar$-curve for $f'(\xi)$ when $n = \mathrm{Re} = m = 1$, $\psi = \epsilon = \gamma = 0.40$, $\alpha = 0.15$, $r^* = 0.2$, $\mathrm{Pr} = 1.5$, $\lambda_1 = 0.5$ and $\beta = 0.25$.

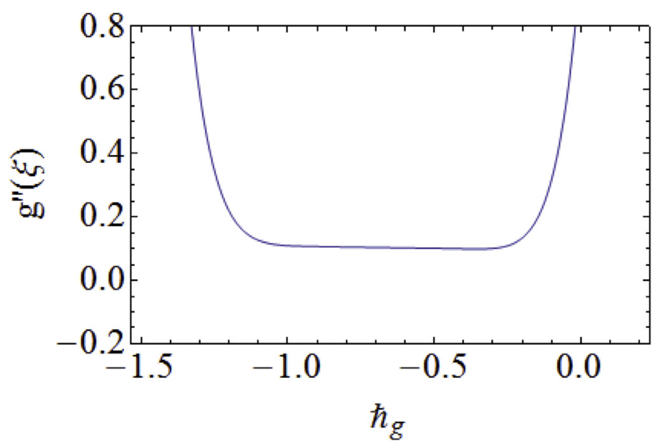

Fig. 3. $\hbar$-curve for $g'(\xi)$ when $n = \mathrm{Re} = m = 1$, $\psi = \epsilon = \gamma = 0.40$, $\alpha = 0.15$, $r^* = 0.2$, $\mathrm{Pr} = 1.5$, $\lambda_1 = 0.5$ and $\beta = 0.25$.

The general solutions $(j_m, f_m, g_m, \theta_m)$ are obtained by solving the system of Eqs. (11)–(16)with the help of corresponding deformations equations and summing up these special solutions $(j_m^*, f_m^*, g_m^*, \theta_m^*)$ as

$$j_m(\xi) = j_m^*(\xi) + a_0, \tag{57}$$

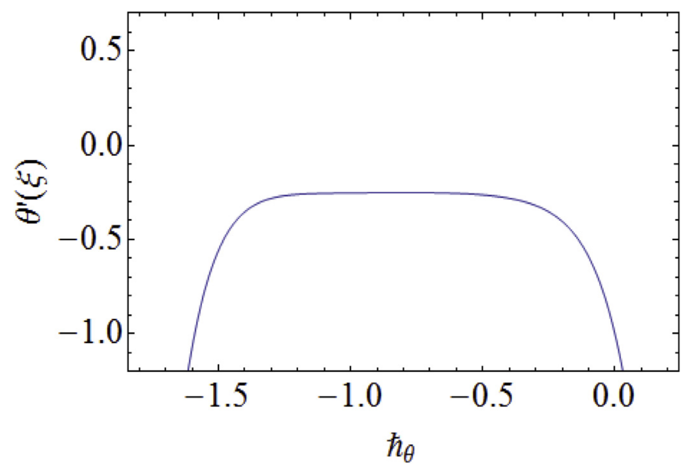

Fig. 4. $\hbar$-curve for $\theta'(\xi)$ when $n = \mathrm{Re} = m = 1$, $\psi = \epsilon = \gamma = 0.40$, $\alpha = 0.15$, $r^* = 0.2$, $\mathrm{Pr} = 1.5$, $\lambda_1 = 0.5$ and $\beta = 0.25$.

$$f_m(\xi) = f_m^*(\xi) + a_1 e^{\xi} + a_2 e^{-\xi}, \tag{58}$$

$$g_m(\xi) = g_m^*(\xi) + a_3 e^{\xi} + a_4 e^{-\xi}, \tag{59}$$

$$\theta_m(\xi) = \theta_m^*(\xi) + a_5 e^{\xi} + a_6 e^{-\xi}. \tag{60}$$

Convergence of the series solution

The technique of homotopy analysis plays significant role in order to obtain and analyze the convergent series solution. Convergence of the series solutions is controlled by introducing the auxiliary parameters. We have used here $\hbar_j$, $\hbar_f$, $\hbar_g$ and $\hbar_\theta$, used as the auxiliary parameter to settle the convergence region. The region of convergence is plotted (see Figs. 1–4) to get ranges of convergent solution. Appropriate ranges for these parameters are $-1.2 \leqslant \hbar_j \leqslant -0.6$, $-1 \leqslant \hbar_f \leqslant -0.6$, $-0.9 \leqslant \hbar_g \leqslant -0.6$ and $-0.9 \leqslant \hbar_\theta \leqslant -0.6$. These solutions are convergent in the full range of ξ for $\hbar_j = \hbar_\theta = -0.8$, $\hbar_f = -0.9$ and $\hbar_g = -0.7$.

Convergence for velocities $j'(\xi)$, $f'(\xi)$, $g''(\xi)$ and temperature $\theta'(\xi)$ is shown in Table 1. The above table is indicating that for the convergence of axial, radial and tangential velocities 36th, 42nd and 28th order of approximations are sufficient respectively. However 47th order of approximation is appropriate for the convergence of $\theta'(\xi)$.

Graphical results

Physical impact of all parameters involved in velocities and temperature is scrutinized in this portion. A concise discussion is made to see how these parameters are influencing the velocities and temperature Beside this an interesting note is added to give a better perception about heat transfer rate of the system under consideration.

Figs. 5–8 show the influence of n, ψ, α and m on $j(\xi)$. Here power law index causes an increase in the velocity $j(\xi)$ as shown in Fig. 5. Since the increasing values of n show a decay in the exponent of radius R_0 and hence the velocity profile increases.For higher values of fluid physical power law exponent n the axial velocity approaches to its asymptotic limit $-h(\infty)$. Fig. 6 depicts the impact of small parameter ψ on axial velocity. It shows that magnitude of axial velocity decreases for increasing values of ψ. Impact of dimensionless coefficient of disk thickness α is portrayed in Fig. 7. Increasing values of α have inverse relation with radius R_0.

Table 1
Convergence of series solutions when $n = \mathrm{Re} = m = 1$, $\psi = \epsilon = \gamma = 0.40$, $\alpha = 0.15$, $r^* = 0.2$, $\mathrm{Pr} = 1.5$, $\lambda_1 = 0.5$ and $\beta = 0.25$.

Order of approximation	$-j'(\xi)$	$f'(\xi)$	$g''(\xi)$	$-\theta'(\xi)$
1	0	0.338	−0.008	0.411
10	0.0315	0.524	0.108	0.254
20	0.0314	0.523	0.111	0.272
28	0.0315	0.525	0.112	0.288
36	0.0316	0.526	0.112	0.298
42	0.0316	0.527	0.112	0.302
47	0.0316	0.527	0.112	0.303
50	0.0316	0.527	0.112	0.303
55	0.0316	0.527	0.112	0.303
60	0.0316	0.527	0.112	0.303

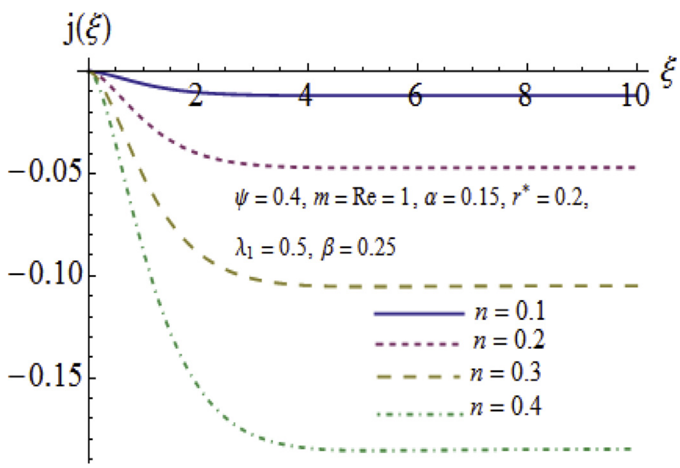

Fig. 5. Influence of n on $j(\xi)$.

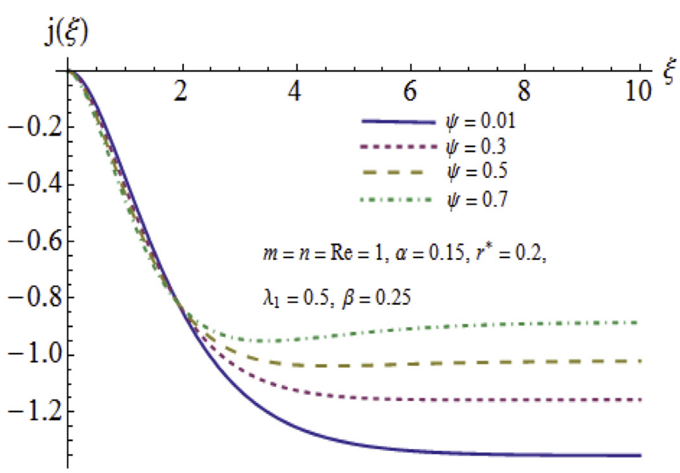

Fig. 6. Influence of ψ on $j(\xi)$.

Hence an increase in disk thickness coefficient reduces the radius. This shows that less fluid particles interact to surface of disk which results increment in velocity. Fig. 8 illustrates the impact of power law exponent of disk thickness m on the axial velocity. It is observed that larger m increase the thickness of the disk and decays magnitude of $j'(\xi)$.

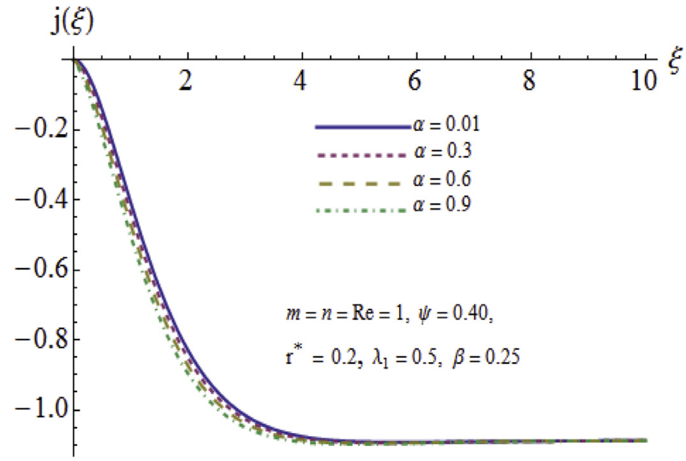

Fig. 7. Influence of α on $j(\xi)$.

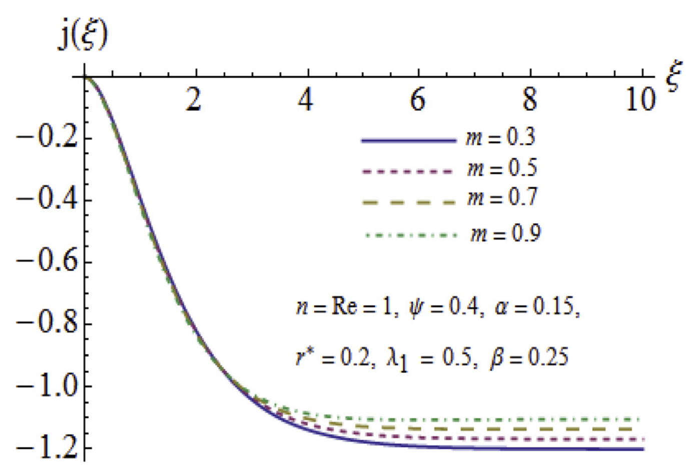

Fig. 8. Influence of m on $j(\xi)$.

Behavior of significant parameters involved in radial velocity field is plotted in Figs. 9–14. Physical impacts of n, Re, α, r^*, ψ and λ_1 on radial velocity is discussed here. Fig. 9 shows the power law index n of fluid effecting the radial velocity. Obviously it can be seen from Fig. 9 that magnitude of velocity enhances for increasing values of n. Fig. 10 depicts the influence of rising values of Re on $f(\xi)$. It is noticed that radial velocity profile has a good increasing behavior for rising values of Re. Since Re is ratio of inertial to viscous forces therefore as we increase the Reynolds number Re the inertial forces dominant and viscous forces produce less resistance to the motion of fluid. Ultimately there is an increase in radial velocity. Fig. 11 demonstrates the effect of α(i.e. dimensionless coefficient of disk thickness) on $f(\xi)$. Here velocity is an increasing function of α. Effect of enhancing values of r^* is portrayed in Fig. 12. Again increment in the values of r^* has inverse relation with radius R_0. Because of minimized radius the radial velocity profile is increasing for r^*. Fig. 13 characterizes that how the radial velocity profile $f(\xi)$ is being influenced by increasing ψ. Radial velocity has direct relation to ψ. Hence magnitude of $f(\xi)$ increases for larger ψ. Influence of λ_1 on radial velocity is illustrated in Fig. 14. Here λ_1 is a ratio of relaxation to retardation times and an increment in this parameter shows that retardation time is decreased. Therefore motion of fluid particle is faster and hence relevant velocity profile increases.

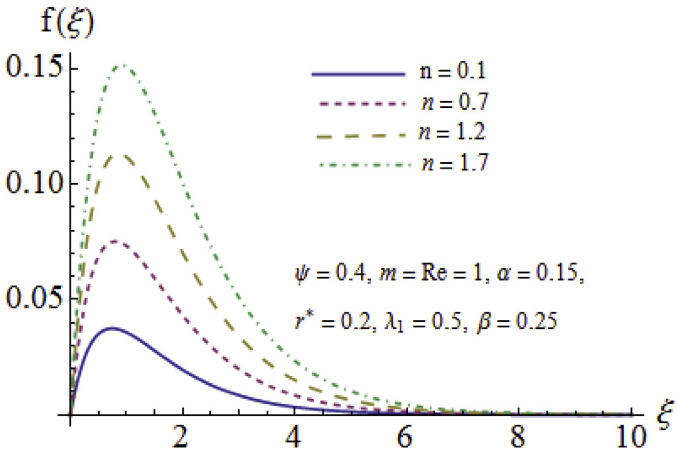

Fig. 9. Influence of n on $f(\xi)$.

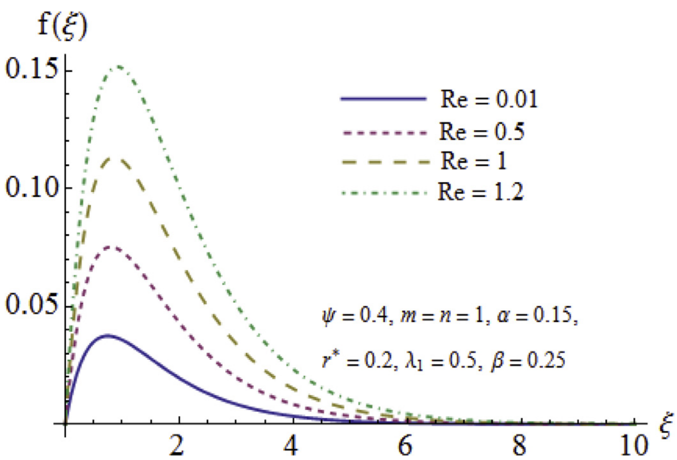

Fig. 10. Influence of Re on $f(\xi)$.

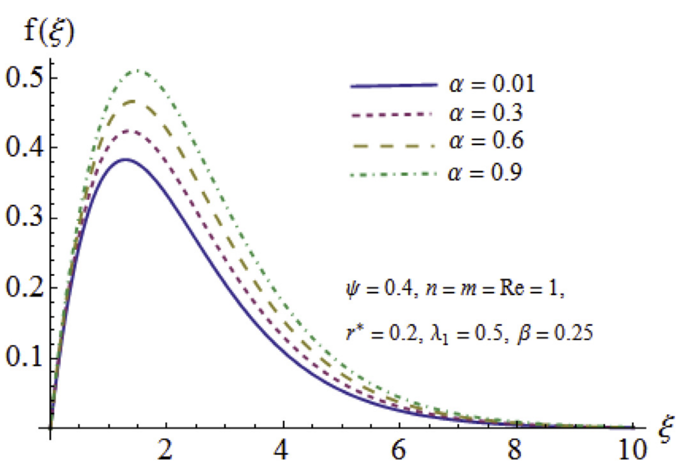

Fig. 11. Influence of α on $f(\xi)$.

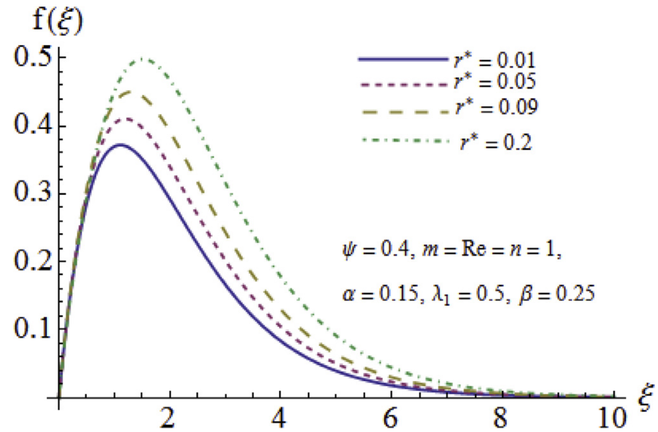

Fig. 12. Influence of r^* on $f(\xi)$.

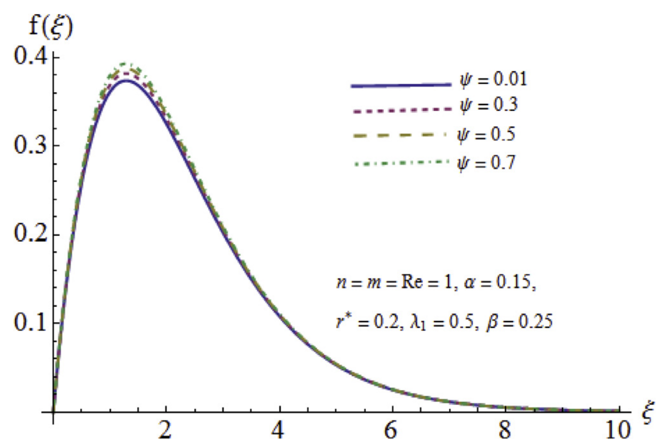

Fig. 13. Influence of ψ on $f(\xi)$.

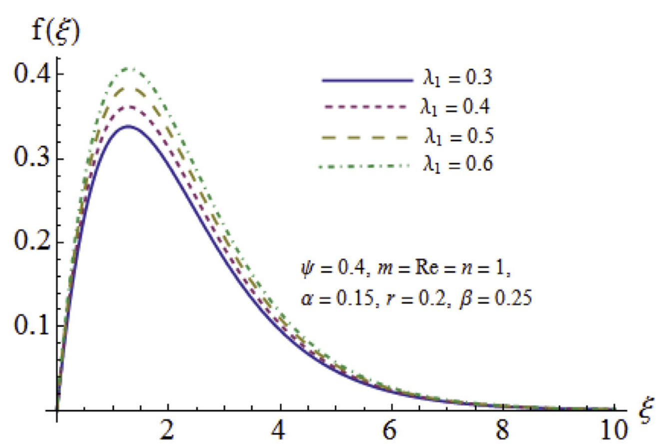

Fig. 14. Influence of λ_1 on $f(\xi)$.

Influence of ψ, Re, r^*, m, λ_1 and β on azimuthal velocity profile $g(\xi)$ is examined in Figs. 15–20. Fig. 15 exhibits that $g(\xi)$ is an increasing function of small parameter ψ. Increasing values of ψ imply reduction in radius R_0 and thus velocity field is increased. Effect of Re on azimuthal velocity is displayed in Fig. 16. Azimuthal velocity $g(\xi)$ rises for larger Re. This is because of the dominance of inertial forces to viscous forces. Thus in view of less viscosity velocity enhances. Fig. 17 indicates the impact of dimensionless radius r^* on azimuthal velocity. This velocity field has a direct relation with r^*. Influence of disk thickness power law exponent m on $g(\xi)$ is shown in Fig. 18. Azimuthal velocity field has direct relation with m. An increase in azimuthal velocity is observed for larger values of m. Impact of λ_1 on $g(\xi)$ is observed in Fig. 19. It is noticed that the magnitude of azimuthal velocity is less for larger values of λ_1. The reason of this behavior is that enlarging values of λ_1 yield intensifying relaxation time for which the fluid particles require

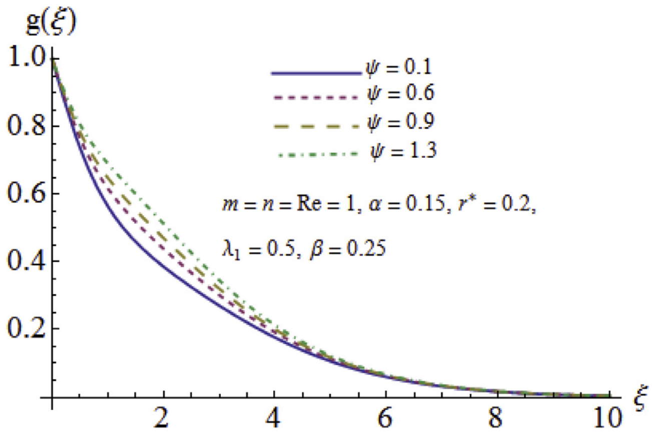

Fig. 15. Influence of ψ on $g(\xi)$.

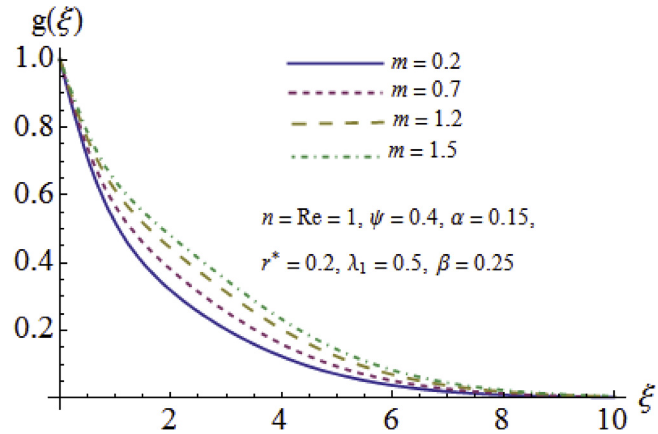

Fig. 18. Influence of m on $g(\xi)$.

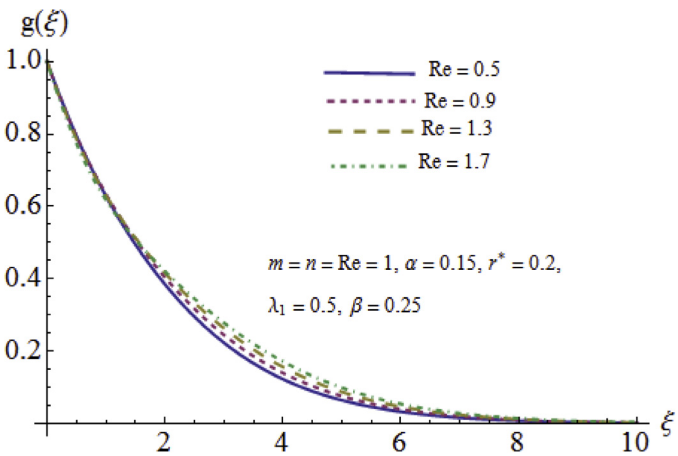

Fig. 16. Influence of Re on $g(\xi)$.

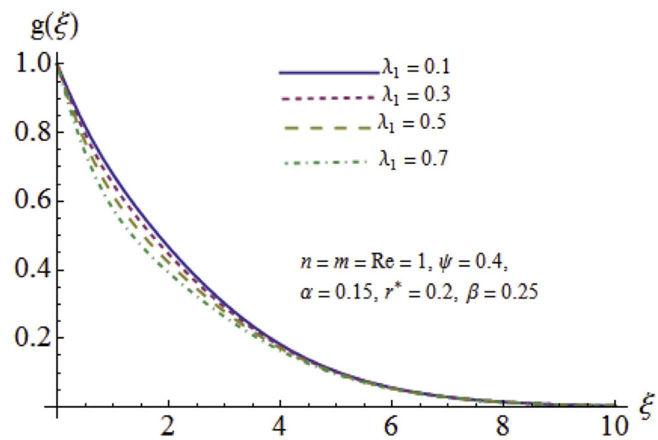

Fig. 19. Influence of λ_1 on $g(\xi)$.

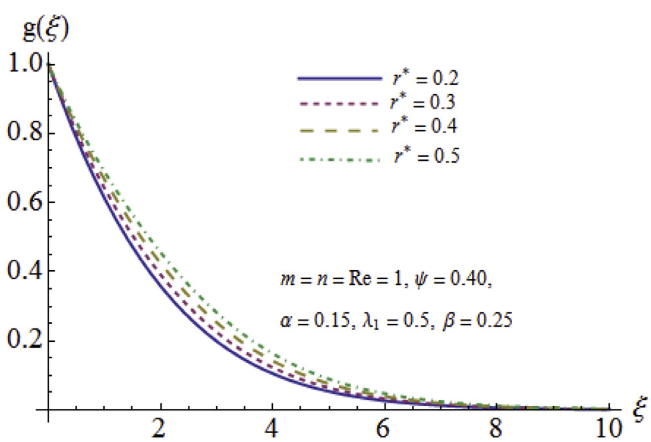

Fig. 17. Influence of r^* on $g(\xi)$.

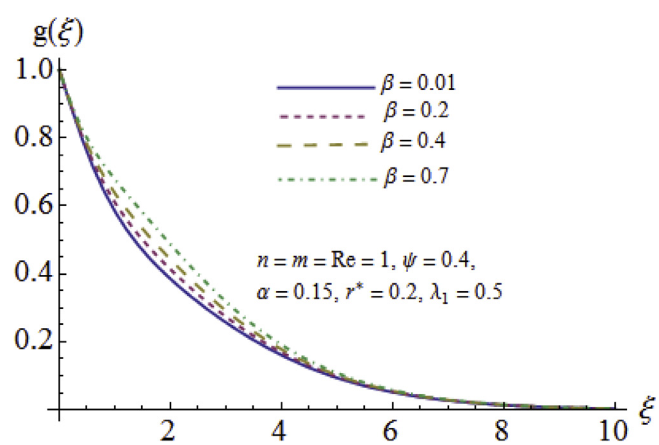

Fig. 20. Influence of β on $g(\xi)$.

additional time to settle down in equilibrium state from the perturbed one. Fig. 20 is designed to show how the azimuthal velocity field is being influenced by Deborah number β. The velocity profile under discussion and corresponding boundary layer thickness are increasing for rising values of β.

Impact of rising values of Reynolds number Re, disk thickness power law exponent m, Deborah number β, Prandtl number Pr, a constant parameter ϵ and thermal relaxation time γ on the temperature field is indicated in Figs. 21–26. Influence of varying values of Reynolds number Re on $\theta(\xi)$ is shown in Fig. 21. This distribution profile and its thermal boundary layer thickness increase for higher Re. Fig. 22 indicates how disk thickness exponent of power law varies the temperature field. The temperature distribution increases for this parameter which physically depicts that heat transfer efficiency is decreased. Fig. 23 depicts that both the thermal boundary layer thickness and temperature field are decreasing when β increases. Physically Deborah number β and relaxation time are directly proportional to each other. Increase in Deborah

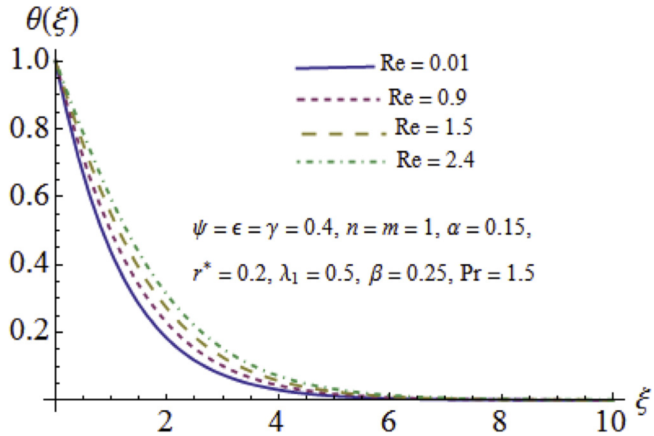

Fig. 21. Influence of Re on $\theta(\xi)$.

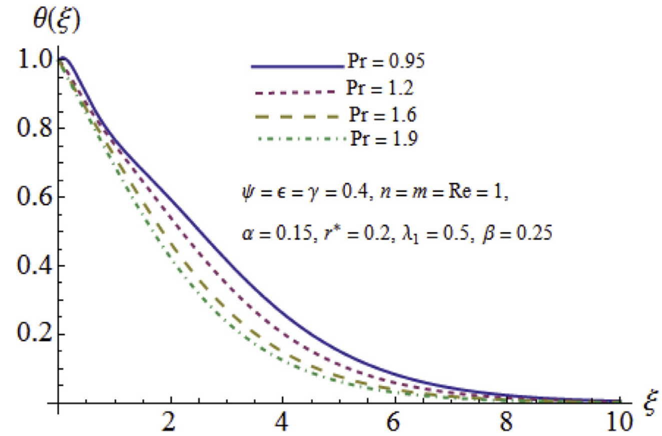

Fig. 24. Influence of Pr on $\theta(\xi)$.

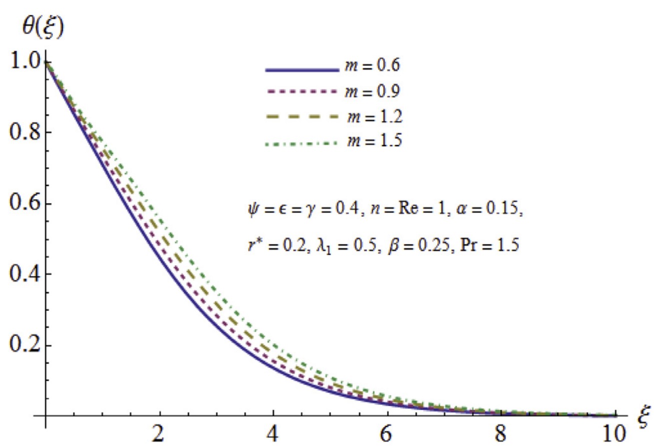

Fig. 22. Influence of m on $\theta(\xi)$.

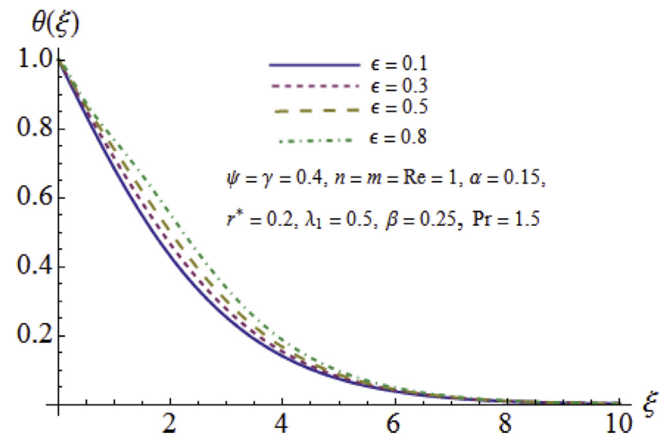

Fig. 25. Influence of ϵ on $\theta(\xi)$.

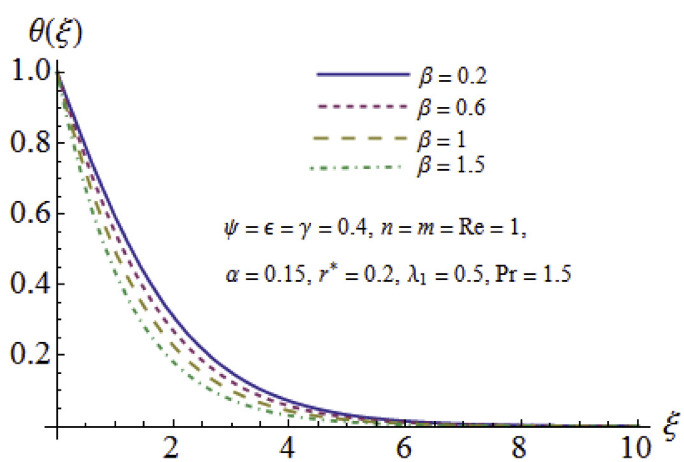

Fig. 23. Influence of β on $\theta(\xi)$.

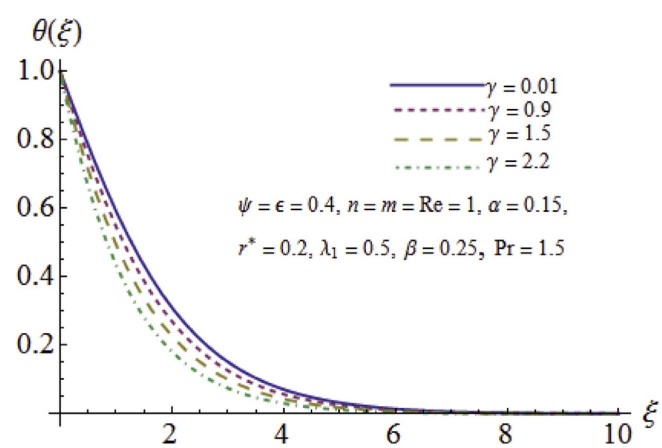

Fig. 26. Influence of γ on $\theta(\xi)$.

number corresponds to higher relaxation time which creates a reduction in temperature. Effect of Prandtl number on thermal boundary layer thickness is displayed in Fig. 24. Rising values of Pr cause a reduction in temperature. It is because that thermal diffusivity becomes smaller for larger Prandtl number which mean fluid particles travel from hot to cold side slowly and hence the temperature reduces. Fig. 25 shows the behavior of a small parameter ϵ on the temperature distribution $\theta(\xi)$. Temperature is an increasing function of ϵ. Finally impact of thermal relaxation time parameter on temperature is represented in Fig. 26. Increase in thermal relaxation time implies particles need more time to transfer heat to neighboring particles and hence the temperature of the system falls. Therefore γ causes reduction in temperature distribution.

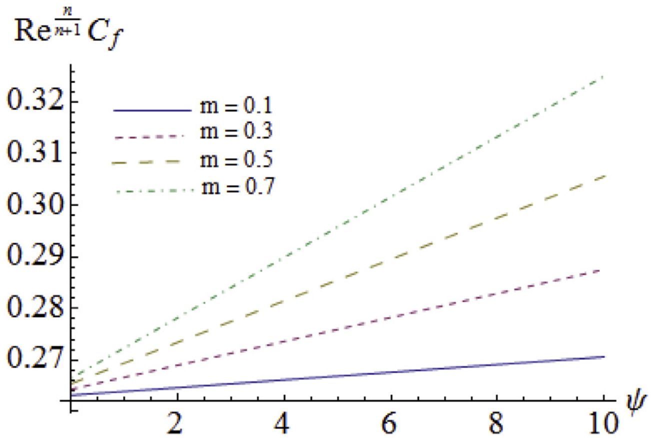

Fig. 27. Influence of m on skin friction coefficient.

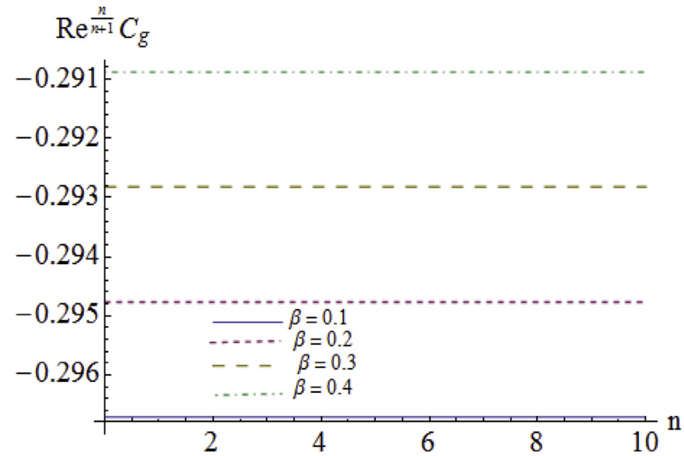

Fig. 30. Influence of β on skin friction coefficient.

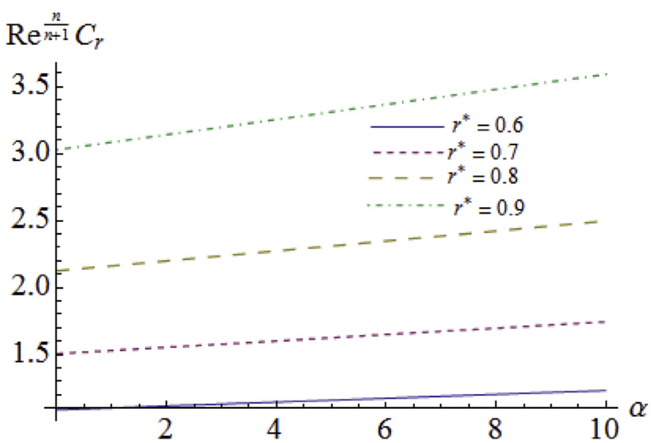

Fig. 28. Influence of r^* on skin friction coefficient.

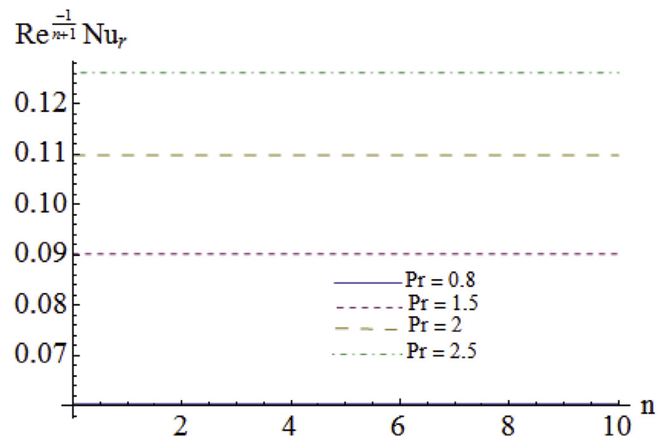

Fig. 31. Influence of Pr on heat transfer rate.

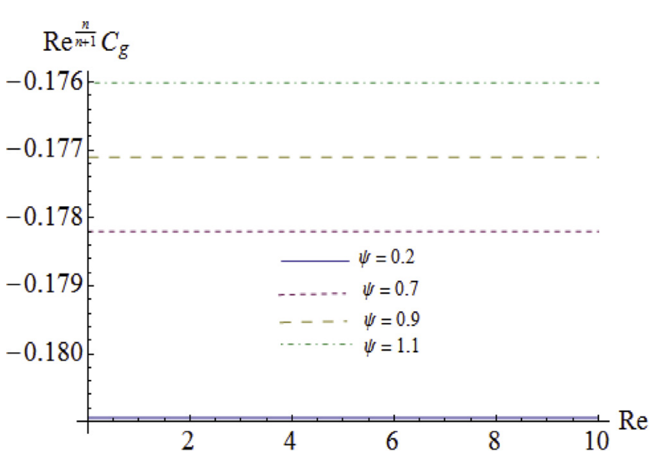

Fig. 29. Influence of ψ on skin friction coefficient.

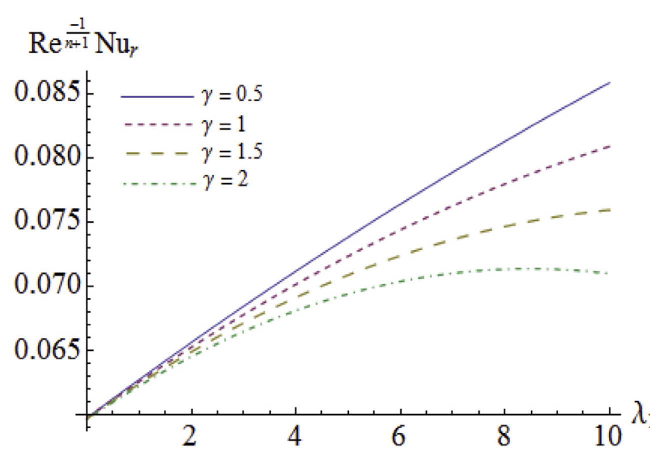

Fig. 32. Influence of γ on heat transfer rate.

Skin friction coefficient and Nusselt number

Graphical interpretations of surface drag force in radial and azimuthal directions are given in Figs. 27–30 respectively. Radial skin friction coefficient is analyzed to see the impact of dimensionless radius r^* and power law exponent m of the disk. However it is seen in Fig. 29 that how a constant parameter ψ effects the surface drag force. Also rising values of Deborah number enhances the tangential skin friction coefficient.

Discussion of heat transfer rate is always an interesting task. Figs. 31,32 are designed to show how heat transfer rate is changing for growing values of Prandtl number and thermal relaxation time.

Conclusions

Here we studied the flow of Jeffrey fluid with Cattaneo-Christov heat flux model and variable thermal conductivity. The main points are.

- Both radial and tangential velocities have decreasing behavior for larger values of ratio of relaxation to retardation times.
- Magnitude of axial and radial velocities rises via power law index of the fluid.
- A constant parameter due to variable thermal conductivity causes an increase in temperature while Deborah number yields opposite reaction.
- Fourier's law gives higher temperature distribution than Cattaneo-Christov heat flux model.
- Surface drag force in tangential direction diminishes for Deborah number while in radial direction it decreases for m and r^*.
- Heat transfer rate decays for larger thermal relaxation time whereas it increases for higher Prandtl number.

References

[1] Rashaida AA, Bergstrom DJ, Sumner RJ. Mass transfer from a rotating disk to a Bingham fluid. ASME J Appl Mech 2005;73(1):108–11.
[2] Sheikholeslamia M, Ellahi R. Three dimensional mesoscopic simulation of magnetic field effect on natural convection of nanofluid. Int J Heat Mass Transfer 2015;89:799–808.
[3] Wenchang T, Mingyu X. Plane surface suddenly set in motion in a viscoelastic fluid with fractional Maxwell model. Acta Mech Sin 2002;18(4):342–9.
[4] Vieru D, Fetecau C, Fetecau C. Flow of a viscoelastic fluid with fractional Maxwell model between two side walls perpendicular to a plate. Appl Math Comput 2008;200(1):459–64.
[5] Fetecau C, Fetecau C. Starting solutions for the motion of a second grade fluid due to longitudinal and torsional oscillations of a circular cylinder. Int J Eng Sci 2006;44(11–12):788–96.
[6] Hayat T, Awais M. Three-dimensional flow of upper-convected Maxwell (UCM) fluid. Int J Numer Methods Fluids 2011;66:875–84.
[7] Ellahi R, Riaz A. Analytical solutions for MHD flow in a third-grade fluid with variable viscosity. Math Comput Modell 2010;52(9–10):1783–93.
[8] Si-Ning Li, Hong-Na Zhang, Xiao-Bin Li, Qian Li. Sang Woo Joo. Numerical study on the heat transfer performance of non-Newtonian fluid flow in a manifold microchannel heat sink. Appl Therm Eng 2017;115:1213–25.
[9] Hakeem AKA, Saranya S, Ganga B. Comparative study on Newtonian/non-Newtonian base fluids with magnetic/non-magnetic nanoparticles over a flat plate with uniform heat flux. J Mol Liq 2017;230:445–52.
[10] Sheikholeslami M, Rashidi MM, Ganji DD. Effect of non-uniform magnetic field on forced convection heat transfer of Fe_3O_4-water nanofluid. Comput Methods Appl Mech Eng 2015;294:299–312.
[11] Attia HA. Rotating disk flow and heat transfer through a porous medium of a non-Newtonian fluid with suction and injection. Commun Nonlinear Sci Numer Simul 2008;13(8):1571–80.
[12] Sahoo B. Effects of partial slip, viscous dissipation and Joule heating on Von Kármán flow and heat transfer of an electrically conducting non-Newtonian fluid. Commun Nonlinear Sci Numer Simul 2009;14(7):2982–98.
[13] Von Karman T. Uber laminare and turbulente Reibung. J Appl Math Mech 1921;1(4):233–52.
[14] Cochran WG. The flow due to a rotating disk. Math Proc Cambridge Philos Soc 1934;30(3):365–75.
[15] Millsaps K, Pohlhausen K. Heat transfer by laminar flow from a rotating plate. J Aeronautical Sci 1952;19(2):120–6.
[16] Turkyilmazoglu M. Flow and heat simultaneously induced by two stretchable rotating disks. Phys Fluids 2016;28. 043601.
[17] Hayat T, Nawaz M, Awais M, Obaidat S. Axisymmetric magnetohydrodynamic flow of Jeffrey fluid over a rotating disk. Int J Numer Methods Fluids 2012;70(6):764–74.
[18] Ming C, Zheng L, Zhang X, Liu F, Anh Vo. Flow and heat transfer of power-law fluid over a rotating disk with generalized diffusion. Int Commun Heat Mass Transfer 2016;79:81–8.
[19] Guha A, Sengupta S. Non-linear interaction of buoyancy with von Kármán's swirling flow in mixed convection above a heated rotating disc. Int J Heat Mass Transfer 2017;108:402–16.
[20] Srinivas S, Reddy AS, Ramamohan TR, Shukla AK. Thermal-diffusion and diffusion-thermo effects on MHD flow of viscous fluid between expanding or contracting rotating porous disks with viscous dissipation. J Egypt Math Soc 2016;24(1):100–7.
[21] Imtiaz M, Hayat T, Alsaedi A, Ahmad B. Convective flow of carbon nanotubes between rotating stretchable disks with thermal radiation effects. Int J Heat Mass Transfer 2016;101:948–57.
[22] Fourier JBJ. Théorie Analytique De La Chaleur. Paris; 1822.
[23] Cattaneo C. Sulla conduzione del calore. Atti Semin Mat Fis Univ Modena Reggio Emilia 1948;3:83–101.
[24] Christov CI. On frame indifferent formulation of the Maxwell-Cattaneo model of finite-speed heat conduction. Mech Res Commun 2009;36:481–6.
[25] Hayat T, Aziz A, Muhammad T, Alsaedi A. Model and comparative study for flow of viscoelastic nanofluids with Cattaneo-Christov Double Diffusion. PLoS One 2017;12(1). 0168824.
[26] Liu L, Zheng L, Liu F, Zhang X. An improved heat conduction model with Riesz fractional Cattaneo-Christov flux. Int J Heat Mass Transfer 2016;103:1191–7.
[27] Meraj MA, Shehzad SA, Hayat T, Abbasi FM, Alsaedi A. Darcy-Forchheimer flow of variable conductivity Jeffrey liquid with Cattaneo-Christov heat flux theory. Appl Math Mech 2017;38(4):557–66.
[28] Reddy JVR, Sugunamma V, Sandeep N. Cross diffusion effects on MHD flow over three different geometries with Cattaneo-Christov heat flux. J Mol Liq 2016;223:1234–41.
[29] Ramesh GK, Gireesha BJ, Shehzad SA, Abbasi FM. Analysis of heat transfer phenomenon in Magnetohydrodynamic Casson fluid flow through Cattaneo-Christov heat diffusion theory. Commun Theor Phys 2017;68(1).
[30] Haddad SAM. Thermal instability in Brinkman porous media with Cattaneo-Christov heat flux. Int J Heat Mass Transfer 2014;68:659–68.
[31] Hayat T, Khan MI, Farooq M, Alsaedi A, Waqas M, Yasmeen T. Impact of Cattaneo-Christov heat flux model in flow of variable thermal conductivity fluid over a variable thicked surface. Int J Heat Mass Transfer 2016;99:702–10.
[32] Abbasi FM, Shehzad SA. Heat transfer analysis for three dimensional flow of Maxwell fluid with temperature dependent thermal conduvitity: application of Cattaneo-Christov heat flux model. J Mol Liq 2016;220:848–54.
[33] Abbasi FM, Mustafa M, Shehzad SA, Alhuthali MS, Hayat T. Analytical study of Cattaneo-Christov heat flux model for a boundary layer flow of Oldroyd-B fluid. Chin Phys B 2015;25.
[34] Shehzad SA, Abbasi FM, Hayat T, Alsaedi A. Cattaneo-Christov heat flux model for Darcy-Forchheimer flow of an Oldroyd-B fluid with variable conductivity and non-linear convection. J Mol Liq 2016;224:274–8.
[35] Eftekhari SA, Jafari AA. Accurate variational approach for free vibration of variable thickness thin and thick plates with edges elastically restrained against translation and rotation. Int J Mech Sci 2013;68:35–46.
[36] Fang T, Zhang J, Zhong Y. Boundary layer flow over a stretching sheet with variable thickness. Appl Math Comput 2012;218(13):7241–52.
[37] Hayat T, Imtiaz M, Alsaedi A. Unsteady flow of nanofluid with double stratification and magnetohydrodynamics. Int J Heat Mass Transfer 2016;92:100–9.
[38] Rashidi MM, Ali M, Freidoonimehr N, Rostami B, Hossian A. Mixed convection heat transfer for viscoelastic fluid flow over a porous wedge with thermal radiation. Adv Mech Eng 2014;204:735939.
[39] Mukhopadhyay S, Ishak A. Mixed convection flow along a stretching cylinder in a thermally stratified medium. J Appl Math 2012;2012:491695.
[40] Tian XY, Li BW, Zhang JK. The effects of radiation optical properties on the unsteady 2D boundary layer MHD flow and heat transfer over a stretching plate. Int J Heat Mass Transfer 2017;105:109–23.